Chapter 18
Thermophysical Properties
of Semiconductors

Yuansu Luo, Bernd Damaschke, Georg Lohöfer, and Konrad Samwer

1 Introduction

The EML facility described in detail in Chap. 3 is actually designed for metallic samples. The processing of semiconductors is therefore a big challenge, because this kind of materials possesses a low electrical conductivity. The laser preheating, which was applied in earlier parabola flight experiments based on the TEMPUS-EML facility [1], is not available in ISS-EML. To overcome this difficulty, we introduced highly doped semiconductors Ge, $Si_{25}Ge_{75}$, and $Si_{50}Ge_{50}$ and processed them recently on board the ISS.

The work has been performed in the framework of the ESA project "SEMITHE RM" ("Investigations of thermophysical properties of liquid semiconductors in the melt and the undercooled state under microgravity conditions," ESA-AO-2000-068). The goals of the project include the precision measurements of the density, thermal expansion, surface tension, viscosity, and electrical resistivity of the liquid Ge and alloys $Si_{1-x}Ge_x$ ($x = 0.75, 0.5$, and 0.25). Due to the strong reactivity of the high-temperature melts, the experiments need to be performed without contact under low-gravity conditions. The Electromagnetic Levitator (ISS-EML) on board of the International Space Station (ISS) is the instrument of choice.

In this chapter, we give an overview over our experiments with semiconductors in ISS-EML. Data from the sample $Si_{50}Ge_{50}$ have already been published in NPJ Microgravity [2] and were taken here for comparison.

Y. Luo · B. Damaschke (✉) · K. Samwer
I. Physikalisches Institut, Georg-August-Universität Göttingen, Göttingen, Germany
e-mail: bdamasc1@gwdg.de

G. Lohöfer
Institut für Materialphysik im Weltraum, Deutsches Zentrum für Luft- und Raumfahrt (DLR), Köln, Germany

2   Sample Preparation, Characterization, and Ground Tests

The samples used are spherical with a diameter of 8 mm, which is the maximal allowed size for samples in the ISS-EML, due to the design of coils. The usage of large spheres is advantageous not only for a sufficient electromagnetic levitation force for relatively low electric conducting samples but also for precision measurements of the droplet size for the evaluation of thermal expansion data. Table 18.1 summarizes the information about the samples used for ISS experiments, including dopant concentration, electrical conductivity (σ), solidus/liquidus temperatures T_s/T_1, and density (ρ).

Here, Ge doped with Sb (donor, n-type) is commercially available, while the $Si_{1-x}Ge_x$ crystals with dopant B (acceptor, p-type) were grown by means of Czochralski technique in the group of N. Abrosimov at the Institute for Crystal Growth in Berlin [3]. A composition gradient along the crystal growth direction is unavoidable due to component segregations. The segregation coefficient for Ge was found to be 0.2 at.%mm^{-1} for $Si_{25}Ge_{75}$ and $Si_{75}Ge_{25}$, and 0.5 at.%mm^{-1} for $Si_{50}Ge_{50}$, corresponding to an uniaxial chemical inhomogeneity of ± 0.8 at.% and ± 2.0 at.%, respectively, for 8 mm spherical samples. The small chemical inhomogeneity does not influence a multicycle processing in ISS-EML.

The dopant concentration of about 10^{19} atoms cm^{-3} for Ge and about 10^{20} atoms cm^{-3} for the alloys corresponds to an electrical conductivity σ in the range of 10^3 Ω^{-1}cm^{-1} at 300 K. Due to the semiconducting behavior, the conductivity of the solid samples rises with T and jumps up to about 10^4 Ω^{-1}cm^{-1} [2] upon melting according to the semiconductor-metal phase transition. Taking frequencies of the heating field (400 kHz) and the positioning field (150 kHz), the skin depths $\delta = \sqrt{2/\sigma\omega\mu}$ (with the angular frequency ω and the magnetic permeability μ) of the eddy currents induced in spherical samples (8 mm) can be estimated to be about 2–3 mm for the solid and 0.8–1.2 mm for the liquid. The large δ (solid) implies a fast heating, while the small δ (liquid) benefits a stable positioning.

Relevant ground tests were made in advance by MUSC (Microgravity User Support Center) at DLR, Cologne, Germany, to obtain relevant parameters, such as spectral emissivity ε for the pyrometer, sample coil coupling efficiency as a measure for the heating capabilities of the doped semiconductors in ISS-EML, as well as the evaporation rate of the melts regarding the limits of dust generation. The spectral emissivity measured for the liquid state was 0.19 for Ge, 0.21 for $Si_{25}Ge_{75}$, and 0.22 for $Si_{50}Ge_{50}$, being about twice smaller than that measured for the solid state (not shown in Table 18.1). The coupling efficiency in the solid state was found to be strong enough for fast heating. In the liquid state, the samples are metallic and the coupling becomes enhanced by a factor of about 5.

In addition, the elements Si and Ge show—similar to water—a density anomaly near T_1 [4]. The phenomenon is already reflected in the density values of the samples listed in Table 18.1. A liquid-liquid phase transformation due to a change of the coordination number of the nearest neighbor atoms in deeply undercooled Si melts has been predicted by Angell et al. [5].

Table 18.1 Summary of sample data (including dopant concentration, solidus/liquidus temperatures T_s/T_l, electrical conductivity σ, spectral emissivity ε, density ρ, values of overheating and undercooling, as well as cooling rates (in 350 mbar Ar) of the melts)

Samples (dopant) (atoms/cm³)	T_s/T_l (K)	Mass of samples (g)	Axial/radial camera (Hz)	Density ρ (gcm⁻³) at RT/T_l	$\sigma(\Omega^{-1}\text{cm}^{-1})$ at RT	Mean overheat (K)	ε (liquid)	Mean (max.) undercooling (K)	Cooling rate (K s⁻¹)
Ge(Sb) $n = 1.0 \times 10^{19}$	1211	1.447	50/200	5.34/5.57	1.0×10^3	430	0.19	65 (81)	4.9
Si$_{25}$Ge$_{75}$(B) $p = 1.5 \times 10^{20}$	1283/1423	1.180	50/400	4.73/5.07	1.3×10^3	340	0.21	20 (25)	13.3
Si$_{50}$Ge$_{50}$(B) $p = 1.9 \times 10^{20}$	1388/1548	1.066	150/400	3.95/4.23	1.7×10^3	370	0.22	165 (245)	12.3
[a]**Si$_{75}$Ge$_{25}$**(B) $p = 1.65 \times 10^{20}$	1533/1623	0.850	150/400	3.15/–	1.4×10^3	390	0.18	143 (245)	27.5

[a]Recently processed on board the ISS in batch #3

3 ISS Experiments in Detail

Before the transport to ISS, the samples were cleaned with acetone and ethanol in ultrasound bath and integrated in a special transport container, which was pumped down to 10^{-7} mbar and filled then with 600 mbar Ar. The end inspection was carried out in air, and thus, the sample surface is unavoidably covered with a natural thin passivation oxide layer, which prevented the sample from further oxidation.

For each semiconductor sample, 11 melting cycles were planned. A cycle consists of heating to a maximal temperature T_{max} and cooling down below T_s, as shown in Fig. 18.1a. At T_{max}, the heater control voltage U_H was set to 0 and the positioner control voltage U_P decreased accordingly from 9 V to 6 V. During the cooling phase, most measurements were executed in argon gas atmosphere (350 mbar). Here, the Ar gas is necessary not only for effective cooling of the sample but also for a reduction of the evaporation rate (mass loss) of overheated melts. A mass loss of about
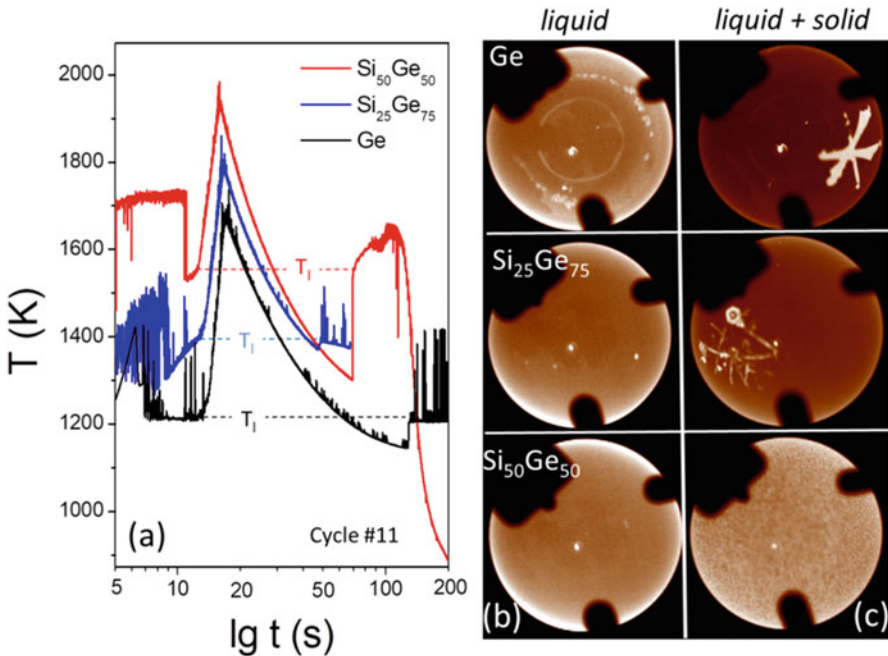

Fig. 18.1 (**a**) Time-temperature profiles (from cycle #11) of Ge (black), $Si_{25}Ge_{75}$ (blue), and $Si_{50}Ge_{50}$ (red) with dashed lines indicating their melting point T_l. (**b**) Axial images recorded at high T (liquid) showing a few residual oxide particles on the surface of the Ge and $Si_{25}Ge_{75}$ droplets. (**c**) Relevant images at beginning of the solidification (liquid + solid) exhibiting strongly heterogeneous nucleation for Ge and $Si_{25}Ge_{75}$ and more homogeneous nucleation for $Si_{50}Ge_{50}$ corresponding to small (black and blue) and large (red) undercooling degrees as shown in (**a**). (Note, the bright spot near the image center comes from pyrometer). (Data for $Si_{50}Ge_{50}$ are taken from Ref. [2])

0.1–0.2 mg per cycle was estimated from the evaporation experiments performed by MUSC.

The surface tension γ and viscosity η of the melt can be determined by the oscillating drop technique (for details, especially the situation with turbulent flow, see "viscosity of the droplet"). For this purpose, several cycles were performed with short pulses of the heating field (triangular pulses 6 or 8 V, 0.05 s) at different temperatures T. The pulse squeezes the drop into an elongated shape along the heating field and results in damped surface oscillations until the sample is back to its equilibrium spherical shape. The exponential decay constant λ of the oscillation amplitude gives the viscosity η of the melt, $\eta = \frac{3M}{20\pi \, r_0} \lambda$ with the mass M and the radius r_0 of the sample, while the resonance frequency ν can be used for the calculation of the surface tension $\gamma = \frac{3\pi M}{8} \nu^2$.

The droplet oscillations were monitored by the axial and radial video cameras. Different camera speeds (cf. Table 18.1) were set depending upon the melting point T_1 of the samples. For Ge (low T_1), for example, the emission of the droplet near T_1 may be dark, and therefore, the speed of axial and radial cameras was set down to 50 Hz and 200 Hz, respectively. The images were analyzed with respect to the above-described oscillating drop method using a dedicated software "TeVi" (SEA Datentechnik GmbH), which detects the droplet edges from the image contrast. The edge curve is fitted with a polynomial of degree 9 [6] and yields areas, radii, and semiaxes of the droplet. From these data also the thermal expansion coefficients β of the sample could be determined.

4   Melting, Cooling, Undercooling, and Solidification Behavior

Doped semiconductors Ge, $Si_{25}Ge_{75}$, and $Si_{50}Ge_{50}$ each with 11 melting and cooling cycles (always the same sample) were successfully processed on board the ISS. Achieved overheats in liquid state are 430 K for Ge, 340 K for $Si_{25}Ge_{75}$, and 370 K for $Si_{50}Ge_{50}$ in average. As an example, Fig. 18.1a reveals their time-temperature plots $T(t)$ of cycle #11 measured by the radiation pyrometer. The sample temperatures T given here were calibrated using Wien's law: $1/T = 1/T_p + (1/T_1 - 1/T_{lp})$ with T_p the pyrometer signal and T_{lp} the pyrometer signal at the liquidus temperature T_1.

As can be seen, in the beginning of the cycles, the temperature reading of the solid samples rises quickly and reaches a plateau corresponding to the solidus temperature T_s, where the sample starts to melt. The $T(t)$-profiles approaching T_s show no significant disturbances, indicating that in spite of a low electrical conductivity, the highly doped semiconductors could be well positioned in the ISS-EML facility. Because of the lower emissivity of the liquid (due to the semiconductor-metal transition, the emissivity changes drastically in the melting process), the temperature reading $T(t)$ drops down during melting and subsequently reaches a minimum, which corresponds to the actual liquidus temperature T_1. The large fluctuation (ΔT

≈ 200 K) of $T(t)$-profiles in the two-phase region arises from the different spectral emissivity ε of the solid and the liquid read by the pyrometer depending on the actual spot, while the small fluctuation ($\Delta T \approx 50$ K) may be due to changes in view factor caused by movement of the sample.

Upon melting, the samples become metallic so that the force applied by the electromagnetic levitation field on droplets grows and improves their positioning stability. As a consequence, $T(t)$-profiles in the liquid state appear very smooth. The low-T_1 sample Ge exhibits a much lower cooling rate and thus a longer cooling phase in comparison with $Si_{25}Ge_{75}$ and $Si_{25}Ge_{75}$ (cf. Fig. 18.1a and Table 18.1). At the end of the liquid phase, where T is usually below T_1 (undercooling), the $T(t)$ profiles rise abruptly up to T_1 (dashed lines in Fig. 18.1a) due to the exothermic nature of the crystallization (not in glassy case).

More interestingly, the red curve in Fig. 18.1a measured for $Si_{50}Ge_{50}$ reveals a large undercooling of about 245 K, associated with the disappearance of surface oxide impurities at high T as discussed below. As one of the advantages of the contactless processing in ISS-EML, the observation of a large undercooling of melts is actually expected. A small undercooling degree was observed however for Ge and $Si_{25}Ge_{75}$, which is attributed to residual oxide phases on the droplet surface.

Figures 18.1b, 18.2b–e, and 18.3b–d show images of Ge, $Si_{25}Ge_{75}$, and $Si_{50}Ge_{50}$ droplets recorded by axial and radial cameras at different T in the liquid state. A few residual oxide particles on the surface of the Ge and $Si_{25}Ge_{75}$ droplets are visible even at T_{max} and become slightly more due to precipitation with decreasing T (cf. Fig. 18.2b–e) in contrast to the $Si_{50}Ge_{50}$ droplet. The residual oxide impurities on the droplet surface serve as additional nuclei for solidification. Figure 18.1c gives relevant images captured at the beginning of solidification (liquid + solid), being dark and bright depending on T_1 of the samples. One can see a strongly heterogeneous nucleation for the droplets Ge and $Si_{25}Ge_{75}$ while the surface of $Si_{50}Ge_{50}$ remains quite smooth. The phenomenon mirrors the quantity of the observed undercooling degrees mentioned above.

For the sample $Si_{25}Ge_{75}$, the strongly heterogeneous nucleation was followed by a dendritic growth (Fig.18.1c, middle) and component segregations. The initially crystalized phase was found to be Si rich (~95 at.%). For pure Ge, the nuclei grew, forming single crystals (diamond lattice) with sixfold symmetry (Fig. 18.1c, upper), i.e., the most dense atomic plans (111). Because of a lower barrier height in the free energy, the heterogeneous nucleation is in general more common than homogeneous nucleation.

For the sample $Si_{50}Ge_{50}$, the rather "homogeneous" nucleation occurs actually for the first time in cycle #6, where the undercooling degree jumps up with no observable dendrite structure. The cycle #1–#5 delivered an undercooling of about 45 ± 10 K only, followed with a heterogeneous nucleation similar to that observed for $Si_{25}Ge_{75}$. The undercooling rises then gradually from 155 K for cycle #6 to 245 K for cycle #11. The results can be attributed to a gradual volatilization of surficial oxide impurities at T_{max} (~1973 K), which is close to the melting point (1986 K) of SiO_2 [7]. In addition, silicon monoxide (SiO) may gradually form at
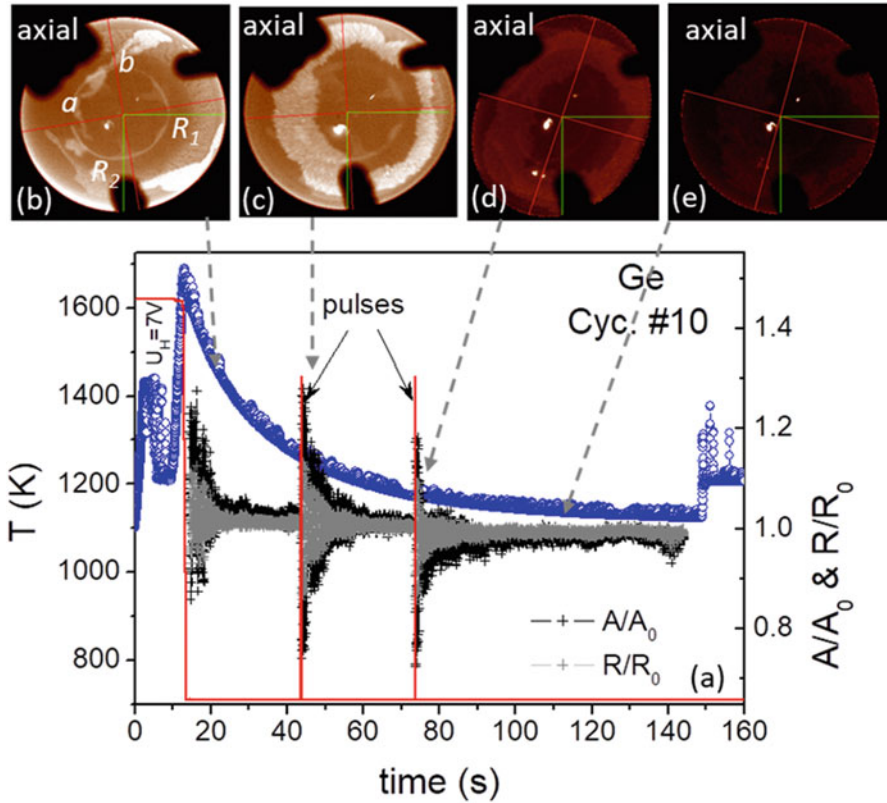
Fig. 18.2 (**a**) Time profiles of cycle #10 measured for Ge with temperature (blue circles), voltage U_H (red line) controlling the electromagnetic heating field with two short pulses used for exciting droplet oscillations, as well as normalized areas A/A_0 (black) and radii R/R_0 (gray). Relevant axial images of the droplet captured between heating-off and the 1st pulse (**b**), at the 1st and 2nd pulses (**c, d**), and far away from the 2nd pulse (**d**), respectively, including semiaxes a, b (red), horizontal and vertical radii R_1, R_2 (green), as well as areas A surrounded by edge curves

high T via a decomposition reaction, $SiO_2 + Si \rightleftharpoons 2\,SiO$. It is volatile and can evaporate away by sublimation [8].

The maximum temperature T_{max} reached for $Si_{25}Ge_{75}$ (Fig. 18.1a) is about 1873 K and is too low to fully resolve the surficial oxide phase. The 11 cycles show a small and almost constant undercooling (20 ± 5 K).
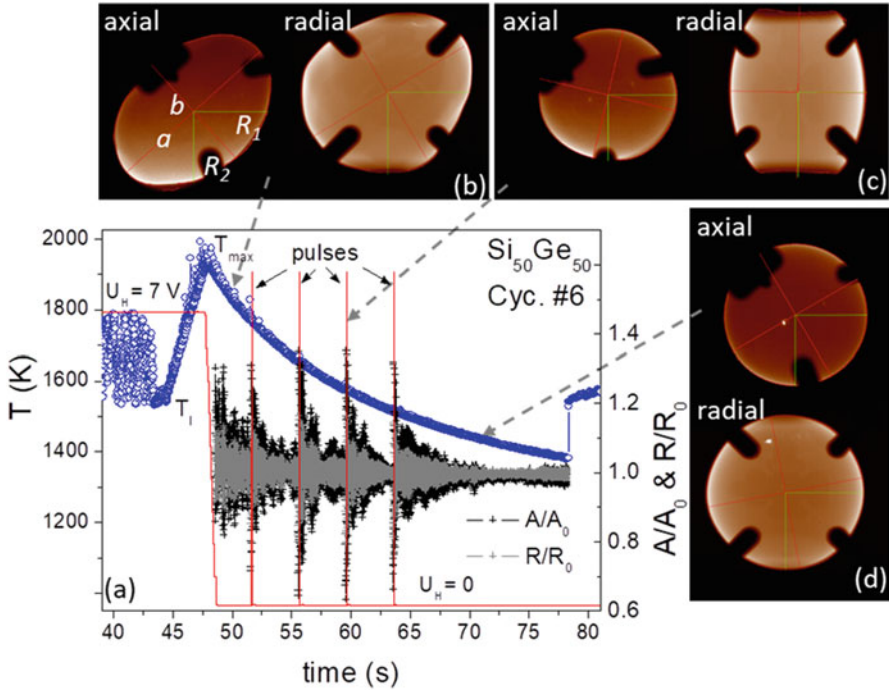
Fig. 18.3 (**a**) Time profiles of cycle #6 measured for $Si_{50}Ge_{50}$ with temperature (blue circles), voltage U_H (red line) controlling the electromagnetic heating field with four short pulses used for exciting droplet oscillations, as well as normalized areas A/A_0 (black) and radii R/R_0 (gray). Relevant axial and radial images of the droplet captured between heating-off and the 1st pulse (**b**), at the 3rd pulse (**c**), and far away from the 4th pulse (**d**), respectively, involving elliptical semiaxes a, b (red), horizontal and vertical radii R_1, R_2 (green), as well as areas A surrounded by edge curves. (Reproduced under the terms of the CC BY 4.0 license [2]. Copyright 2020, Springer Nature)

5 Oscillating Drop Method and Evaluations

Figures 18.2b–e and 18.3b–d show typical axial and radial images measured for Ge and $Si_{50}Ge_{50}$ at different points indicated in relevant $T(t)$-plots given in Figs. 18.2a and 18.3a, respectively. The Ge droplet became very dark for T below T_l. The shadowlike artifacts stem from parts of the sample holder, and their areas have been excluded in the edge fitting procedure. The digital procedure yields data of areas A and lengths of horizontal and vertical radii R_1 and R_2 as well as elliptical semiaxes, a and b, as a function of time and temperatures for evaluation of thermophysical properties via the oscillating drop method.

To minimize the scattering of data, we introduced an average radius R calculated from R_1, R_2, a, b, and r_{eff}, where r_{eff} is an effective radius extracted from the area $A = \pi r_{eff}^2$. The normalized areas A/A_0 and radii R/R_0 with A_0 and R_0 denoted as their mean values are plotted in Figs. 18.2a and 18.3a, showing damped oscillations

caused by switching off the electromagnetic heating field, which also squeezes the droplet, and short voltage pulses.

As illustrated in Fig. 18.3c, the short pulse (8 V, 0.05 s) squeezes the drop into a more elongated shape along the perpendicular axis. The cross section viewed from the top in axial direction correspondingly becomes smaller and in radial direction looked incomplete due to a hiding effect of the electromagnetic coil (its winding distance is 8 mm). The uniaxially deformed droplet relaxes to its equilibrium spherical shape, giving rise to surface oscillations. A similar behavior appears at T_{max} by turning off the heating. In this case, the uniaxial deformation is however much stronger than that induced by short pulses, giving rise to rotation of the droplet around an arbitrary axis with a period of about 1 Hz (see Fig. 18.3a). The overlap between rotation and oscillation makes the droplet temporarily aspherical (Figs. 18.2c, d, and 18.3b, c) and leads to extra scattering of the experimental data. Only for long times after the heating-off or pulses, the droplet becomes quiet and well spherical, as shown in Figs. 18.2e and 18.3d. For this case, all length data a, b, R_1, and R_2 are nearly identical and the scattering becomes smaller. The pulse height used for Ge was set down to 6 V to reduce the uniaxial deformation.

6 Viscosity of the Droplet

Typical oscillations of levitated Ge and Si-Ge droplets excited at different T by switching the heater off at T_{max} and by heating pulses are presented as a function of the time t in Figs. 18.2a, 18.3a, and 18.4a, c, e. The amplitude decays exponentially with t and approaches then the mean value A_0 (or R_0). The behavior can be fitted by $f = f_0 \pm \Delta f \cdot e^{-\lambda t}$; here, f/f_0 can be A/A_0 or R/R_0, and Δf is their maximal amplitude. The fit provides the envelope of the oscillation as plotted in Fig. 18.4a, c, e (red dashed lines) and yields a decay factor λ, which in the case of laminar flow can be referred as the magnitude of the viscosity, i.e., $\eta = \kappa \lambda$ [9]. Here, $\kappa = \frac{3M}{20\pi\, r_0}$ with the radius $r_0 = 4$ mm and the mass M of the droplets. In the case of the semiconductor samples discussed here, the fluid flow is turbulent and the model is not strictly applicable. Instead, we have evaluated the decay factor λ; for details, see the discussion below.

The red dashed lines in Fig. 18.4a demonstrate the envelopes fitted with exponential function of $e^{-\lambda t}$ from the oscillation data obtained from cycle #5 (axial) for Ge. The given oscillations were excited by four short pulses at 1658, 1553, 1473, and 1418 K with decay factors λ found to be in the order of 0.30 s^{-1}. Because of the small interval (4 s) between two pulses, the oscillations induced by the 1st, 2nd, and 3rd pulses decay not completely before the next pulse started (see also Fig. 18.3a). This makes the fitting more difficult; additionally, a rotation of the droplet creates a parasitic oscillation of about 1 Hz (near the pulses) and disturbs the direct observation of the decay behavior. Therefore, the fitting procedure is delicate and not all pulses could be fitted well. Fig. 18.4c, e show the fits of the oscillation data obtained
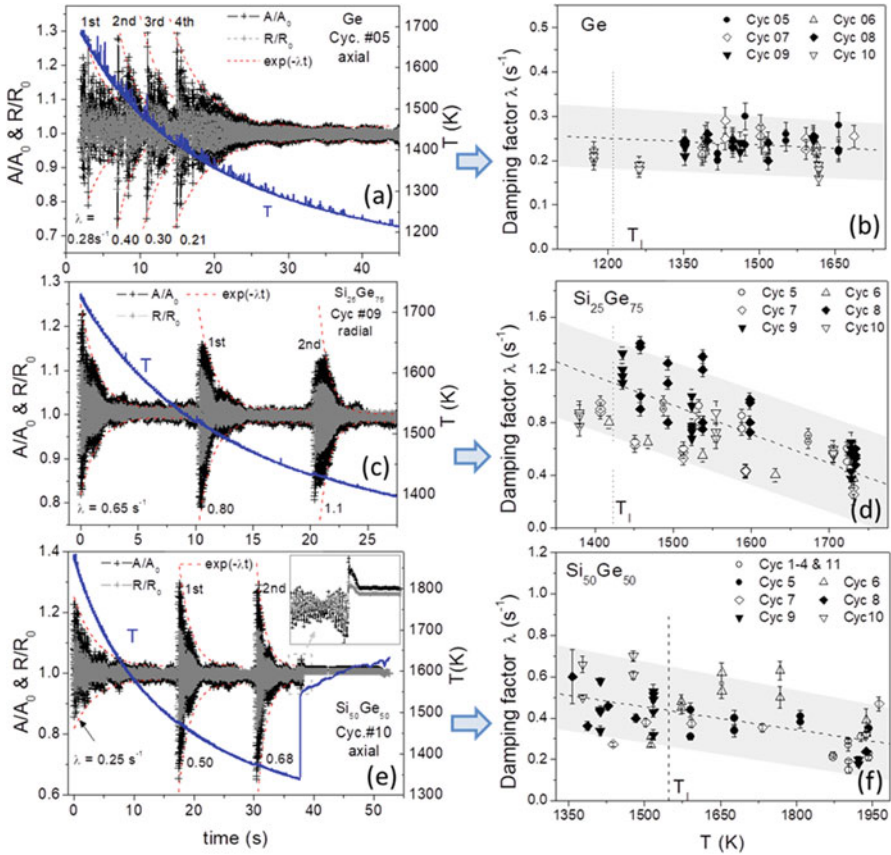
Fig. 18.4 (**a**), (**c**), and (**e**): $T(t)$ profiles (blue) measured for Ge (cycle #5, axial), $Si_{25}Ge_{75}$ (cycle #9, radial), and $Si_{50}Ge_{50}$ (cycle #10, axial) with normalized areas A/A_0 (black) and radii R/R_0 (gray) revealing oscillations excited by heating-off and short pulses (marked here by 1st, 2nd, and 3rd...), respectively, and decayed with t in an exponential function $e^{-\lambda t}$ (red dashed lines), as well as abrupt changes (inset in e) occurring upon solidification regarding the density anomaly mentioned [6]. (**b**), (**d**), and (**f**): Damping factors λ of the oscillations measured for relevant samples from pulse cycles. Note, here different λ-scales indicate different T dependence. The gray background indicates the scattering of ± 0.1–0.3 s^{-1}. The week T dependence is probably due to the influence of the turbulent flow. (Data for $Si_{50}Ge_{50}$ are taken from Ref. [2])

from the alloy droplets $Si_{25}Ge_{75}$ (radial, cycle #9) and $Si_{50}Ge_{50}$ (axial, cycle #10). The oscillations shown here were caused by heating-off and two short pulses (interval ~10 s). The impact from the rotation is visible as well. As indicated in Fig. 18.4e, for $Si_{50}Ge_{50}$, two pulses are located below T_l, but the oscillation behavior is similar to that observed above T_l.

Figure 18.4b, d, f gather the damping factors λ of the oscillating droplets Ge, $Si_{25}Ge_{75}$, and $Si_{50}Ge_{50}$ at different T from data of pulse cycles. They are weakly temperature dependent and do not show an Arrhenius-type behavior [10]. For

comparison, we drew schematically dashed lines in Fig. 18.4b, d, f, which present mean values and can be expressed by a fitting function $\lambda = \lambda_0 - \alpha \cdot 10^{-4}(T - T_l)$ with λ_0 denoted as damping factor at the liquidus temperature and α as the slope. We found thereby $\lambda_0 = 0.25$, 1.1, and 0.5 (s^{-1}) and $\alpha = 0.5$, 22, and 3.5 ($\text{K}^{-1}\text{s}^{-1}$) for Ge, $Si_{25}Ge_{75}$, and $Si_{50}Ge_{50}$, respectively. The results might suggest an alloying effect, i.e., the damping (near T_l) of the pure Ge is lower than that of two alloys. Accordingly, the temperature dependence of the damping is less pronounced for Ge ($\alpha = 0.5$) in comparison with the two alloys ($\alpha = 22$ and 3.5). The slope α observed for $Si_{25}Ge_{75}$ is about six times larger than that for $Si_{50}Ge_{50}$. The phenomenon implies that, on the one hand, the alloying effect is possibly nonlinear with Si content in Ge and, on the other hand, an additional influence from the residual oxide phase on the surface may be possible as discussed above.

For a discussion of the viscosity data measured here by the oscillating drop method, the fluid flow in the droplets plays a crucial role. In EML facility, even a low positioning field (here 6 V) could lead to turbulent flow in a low viscosity droplet and therefore to an enhanced damping [11]. Qualitatively, the turbulent behavior can be observed by the movements of oxide particles, which exist on the surface (for $Si_{50}Ge_{50}$ in the first five cycles). Particles of about 50–100 μm in size could be tracked in video images. They circulate or move chaotically on the droplet surface with maximum observed velocities V of about 0.12 m s^{-1}. The Reynolds number R_e, which is defined as the ratio of inertial force $\frac{\rho V^2}{L}$ to viscous force $\frac{\eta V}{L^2}$ (ρ is the density of the droplet and L its characteristic dimension), i.e., $R_e = \frac{\rho V L}{\eta}$ [12], can be estimated to be $R_e \geq 4800$, taking $\rho = 5.0$ g cm^{-3} (for Ge and two alloys in average), $L = 8$ mm (diameter of the sample), and the viscosity η assumed to be $\leq$ 1 mPa·s as measured in experiments with an electrostatic levitator (ESL) [11, 13, 14]. Moreover, a detailed fluid flow modeling was made for the Ge droplet in the group of R. W. Hyers, Univ. of Massachusetts, and resulted in even higher Reynolds numbers of about 6500–70000 [15].

A further indication of the turbulent flow is the dynamical behavior of the droplet surface, showing self-excited oscillations during the whole cooling phase, as can be seen in Figs. 18.2, 18.3, and 18.4.

These findings lead to the conclusion that the measured damping factor λ may be dominated by the levitation force-induced fluid flow, and as a result, the relevant viscosity may deviate from the molecular viscosity measured in other experiments on earth. The argumentation is supported by the smaller value of $\eta < 1$ mPa·s measured for similar samples in an ESL [13, 14].

In addition, the molecular viscosity η may be estimated roughly by its relation to the surface tension γ as suggested by Egry et al. [16, 17], namely, $\frac{\gamma}{\eta} = 0.94\sqrt{\frac{RT}{W}}$, where R is the molar gas constant (8.314 J mol^{-1}K^{-1}) and W the molecular weight. In principle, this form provides an opportunity to separate the temperature dependence of the damping into turbulent and laminar flow. Though the form is valid strictly only for pure elements and simple metallic liquids, we have taken it for estimating the order of magnitude of the molecular viscosity. For example, for
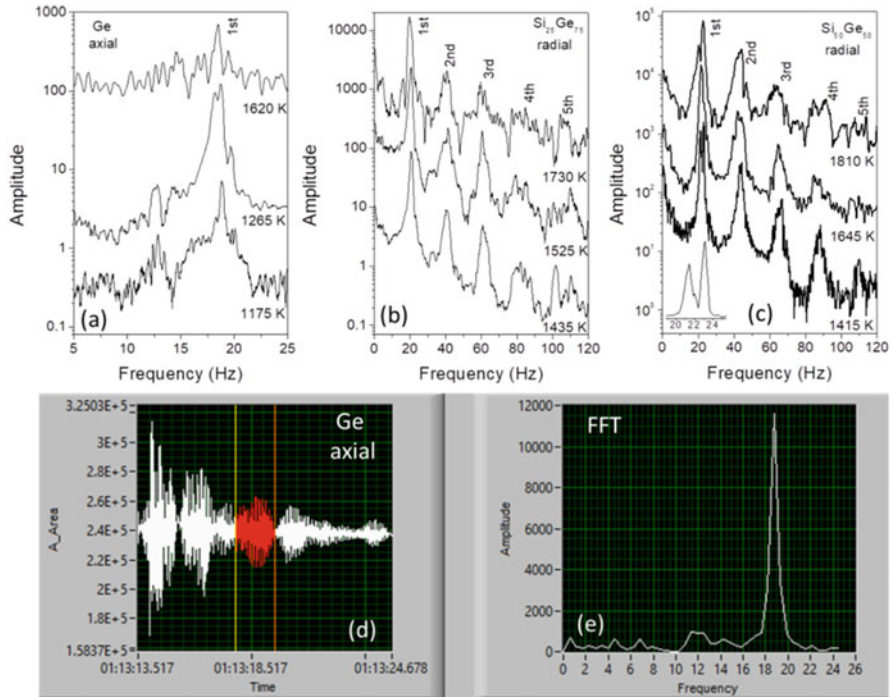
Fig. 18.5 (**a**), (**b**)**,** and (**c**) Frequency spectra obtained from oscillations of the droplets Ge, $Si_{25}Ge_{75}$, and $Si_{50}Ge_{50}$ induced at different T. Inset in (**c**), splitting of the resonance peak arising from droplet rotations. (**d**) and (**e**) Time-segmental FFTs of oscillation data to minimize the impact from parasitic oscillations. (Data for $Si_{50}Ge_{50}$ are taken from Ref. [2])

$Si_{50}Ge_{50}$, with $W = 50.35$ g mol^{-1} and $\gamma = 0.6$ N m^{-1} measured near T_1 (cf. Fig. 18.6c), we get a value η of about 1.2 mPa·s supporting the discussion above.

7 Surface Tension of the Droplet

To determinate the surface tension γ of the droplets, the frequency spectra were deduced from the relevant oscillation data by means of fast Fourier transform (FFT). Figure 18.5a–c exhibit FFT frequency spectra obtained from oscillations of the droplets Ge, $Si_{25}Ge_{75}$, and $Si_{50}Ge_{50}$ excited by heating-off and short pulses at different temperatures. The occurrence of resonance peaks of the 1st order at about $\nu = 18$, 20, and 22 Hz can be seen, respectively, including higher harmonic peaks. The difference of the 1st peak positions partly mirrors the different masses M of the samples. The maximum frequency of FFT spectra shown in Fig. 18.5a–c depends on camera speeds. It is therefore smaller (~25 Hz) in Fig. 18.5a due to the usage of the low-speed axial camera (cf. Table 18.1).

Fig. 18.6 Surface tensions γ measured at different temperatures for Ge (**a**), $Si_{25}Ge_{75}$ (**b**), and $Si_{50}Ge_{50}$ (**c**), dashed lines drawn in view of the average. The lower values indicated by arrows (in **a**, **c** only for the cycle #9 and in **c** for cycle #6) are associated with highly deformed droplets at beginning of excited oscillations. (Data for $Si_{50}Ge_{50}$ are taken from Ref. [2])
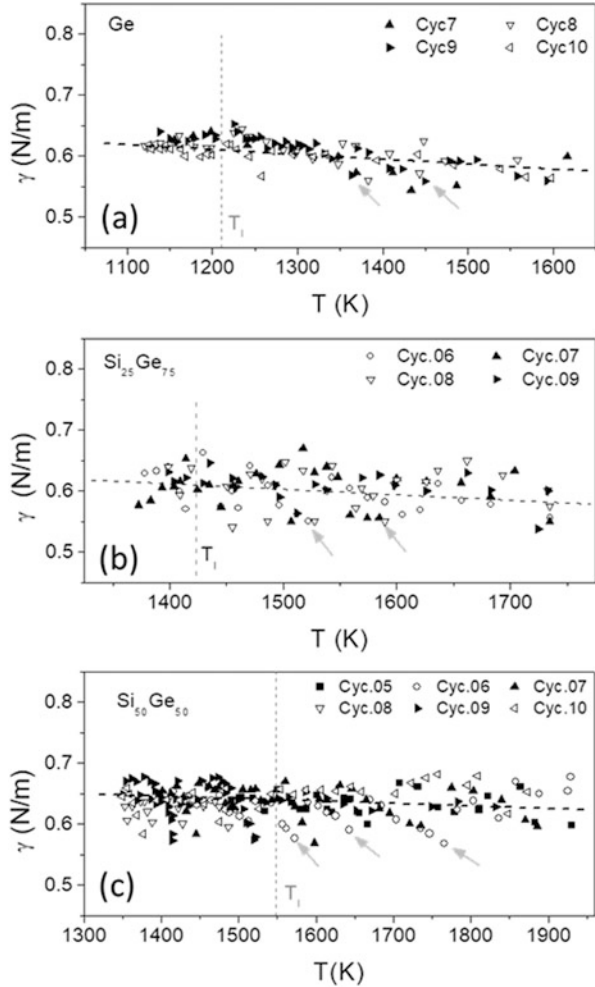
For each sample, temperature dependences are here visible, i.e., the resonance peaks are shifted slightly toward higher frequency for decreasing temperature. Since $\gamma = \frac{3\pi M}{8}\nu^2$ [9], this result implies an increase of γ for decreasing temperature.

Parasitic oscillations arising essentially from the droplet rotation (~1 Hz) are overlapped with the surface oscillation, leading to a splitting of the resonance peaks (also see the inset in Fig. 18.5c) and have to be taken into account by the evaluation of the resonance frequency. To minimize the impact from the parasitic oscillations, we have to operate the FFTs segmentally, as demonstrated in Fig. 18.5d. By means of a careful division, a segmentation of data yields a frequency spectrum with a single, nearly symmetrical resonance peak (Fig. 18.5e). A series of γ values as function of the temperature were extracted in this manner and are plotted versus T in Fig. 18.6a–c, where dashed lines are drawn in view of the average. The linear

T dependence can be approximately written as $\gamma = \gamma_0 - \xi \cdot 10^{-5}(T - T_1)$ with γ_0 as the value at the melting point and ξ as the slope. We got $\gamma_0 \approx 0.61$ N/m, $\xi \approx 8$ N/m·K for Ge, $\gamma_0 \approx 0.61$ N/m, $\xi \approx 9$ N/m·K for $Si_{25}Ge_{75}$, and $\gamma_0 \approx 0.65$ N/m, $\xi \approx 4$ N/m·K for $Si_{50}Ge_{50}$, respectively. Note, the slope ξ of $Si_{25}Ge_{75}$ is here slightly larger than that of $Si_{50}Ge_{50}$ by a factor of about two, being dissimilar to the relevant slopes of λ versus T given in Fig. 18.4d, f, different by a factor of about 6. This remarkable observation may be caused by a surface effect, but this interpretation has to be confirmed by additional measurements in the future.

In addition to errors caused by splitting or asymmetrical behavior of the resonance peak due to droplet rotation, the deformation (δ) of the droplet may give rise to a frequency shift, $\frac{\Delta \nu}{\nu} = p_1\delta + p_2\delta^2$, as recently investigated by Xiao et al. [18]. Here, the constant p_1 and p_2 are negative and the frequency shifts thus toward lower values. This nonlinear behavior is also visible here and even pronounced at the beginning of excited oscillations as indicated by arrows in Fig. 18.6. The deformation amplitude δ of the molten Ge, $Si_{25}Ge_{75}$, and $Si_{50}Ge_{50}$ can be estimated from the R/R_0 data shown in Figs. 18.2a, 18.3a, and 18.4a, c, e. It is about 15% at the beginning of the excited oscillations and decreases rapidly with t. After 1–2 s, δ becomes below 10%. Though it is slightly above the limit ($\delta = 7\%$) reported in Ref. [18], the equation mentioned above for the surface tension is only approximately valid.

The measured surface tension is comparable to published data in the literature. In previous parabola flight experiments with undoped Si-Ge samples [19] and doped Si-Ge samples with rich Ge-content [6], the values and the temperature dependences are similar. Measurements with an ESL also lie in the same range [14]. Experiments with the pendant drop method on earth show similar values [20].

8   Thermal Expansion

Figure 18.7a, b show normalized values of A/A_0 and R/R_0 obtained from the droplets of Ge (cycle #1) and $Si_{25}Ge_{75}$ (cycle #9), respectively. To optimize the accuracy of the thermal expansion data, largely scattered data beyond $\pm10\%$ deformation arising from strong deformations of the droplets during the heating-off and short pulse period (about 1–2 s) were removed. Figure 18.7c shows the data obtained from the deeply undercooled droplet $Si_{50}Ge_{50}$ (cycle #11 with no pulse), showing very low scattering of 1 ± 0.02 much smaller than those given in Fig. 18.7a, b.

Linear fitting of these data yields coefficients $\beta_A = A^{-1}dA/dT$ (A = area) and $\beta_R = R^{-1}dR/dT$ (R = radius) of area and linear thermal expansion in given temperature ranges. The error values in brackets shown in Fig. 18.7a–c give the uncertainty of the linear fit. As expected, β_A is found here to be nearly equal to $2\beta_R$. It should be mentioned that the β values given in the plots are taken from different T-ranges, but in general, they become higher at higher temperatures. For example, the deeply undercooled droplet $Si_{50}Ge_{50}$ reveals the lowest coefficients ($\beta_A = 4.25 \times 10^{-5}$ K^{-1}
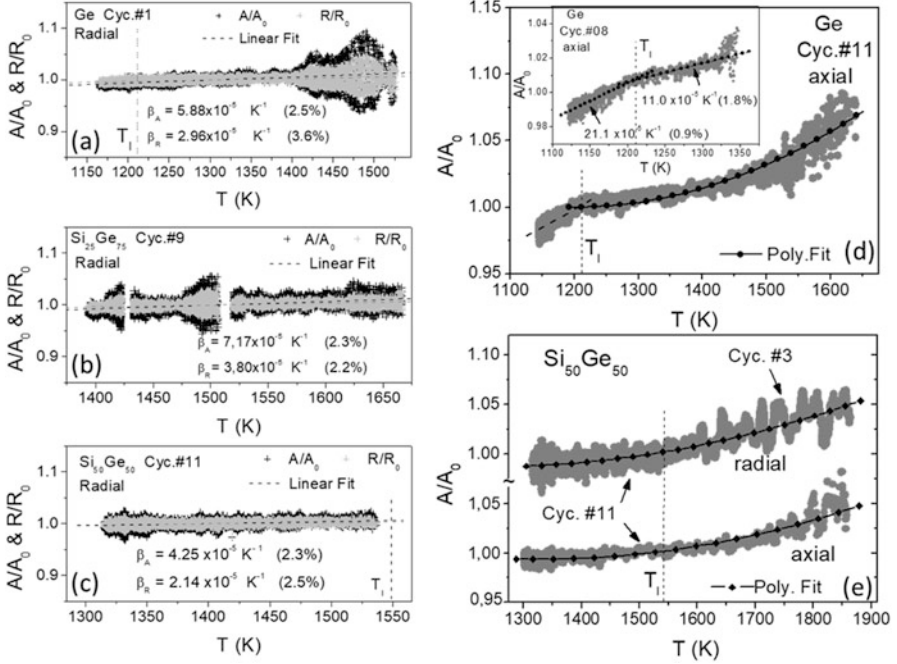
Fig. 18.7 (**a**), (**b**), and (**c**) Normalized radial areas A/A_0 and radii R/R_0 as a function of T measured for Ge (cycle #1), $Si_{25}Ge_{75}$ (cycle #9), and $Si_{50}Ge_{50}$ (cycle #11), linear fits give coefficients of the thermal expansion β_A (area) and β_R (radius) in given T ranges. (**d**) Axial data of Ge from cycles #11 and #8 (inset) and (**e**) axial and radial data of $Si_{50}Ge_{50}$ from cycles #3 and #11, showing a nonlinear behavior, which can be approximately fitted by a 2nd-order polynomial. As a special feature, the droplet Ge shows a nearly twice larger slope below T_l. (Data for $Si_{50}Ge_{50}$ are taken from Ref. [2])

and $\beta_R = 2.14 \times 10^{-5} \text{ K}^{-1}$) as given in Fig. 18.7c, being much lower than those ($\beta_A = 10.0 \times 10^{-5} \text{ K}^{-1}$ and $\beta_R = 4.9 \times 10^{-5} \text{ K}^{-1}$) obtained from the same sample but highly overheated run from 1550 to 1875 K. The result suggests a nonlinear thermal expansion of the liquid.

To show this in more detail, Fig. 18.7d, e exhibit relevant axial/radial video data measured for the droplets Ge and $Si_{50}Ge_{50}$, covering both overheating and undercooling temperature ranges. Note that in Fig. 18.7e, the radial data of cycle #11 is combined here with the radial data of cycle #3, due to the limited data storage capacities on board the ISS and thus a restricted length ($\leq$30 s) of radial image video data (400 Hz). In addition, to minimize the scattering, smoothing of the data were done by adjacent averaging. A nonlinear behavior of the droplet sizes with T is apparent and can approximately be fitted here by a 2nd-degree polynomial R/R_0 $(T) = \alpha_R + \beta_{R0}(T - T_l) + \beta_R{'}(T-T_l)^2$ or $A/A_0 = \alpha_A + \beta_{A0}(T - T_l) + \beta_A{'}(T - T_l)^2$ with constants $\alpha_{R, A}$ close to 1. Differential operation of the equation yields thermal expansion coefficients as a linear function of T, namely, $\beta_{R, A} = \beta_{R, A0} + 2\beta_{R, A}{'}(T - T_l)$ where $\beta_{R, A0} \approx 10^{-5} \text{ K}^{-1}$ as initial value at T_l and $2\beta_{R, A}{'} \approx 10^{-7} \text{ K}^{-2}$ as the slope.

With the help of the equation, the β_R value near the liquidus temperature T_1 can be evaluated. Averaging over all cycles, for example, we get a mean β_R of about 3.15×10^{-5} K^{-1} for $Si_{50}Ge_{50}$. For $Si_{25}Ge_{75}$, which showed a small undercooling (~20 K), the mean values of β_A and β_R were found to be about 6.35×10^{-5} K^{-1} and 3.20×10^{-5} K^{-1}, respectively.

More interestingly, a special feature was observed for pure Ge, namely, below T_1, the droplet decreases in size with decreased T nearly twice faster than above T_1, as can be followed in Fig. 18.7d or inset. For this situation, we had to fit the data ($T > T_1$), and obtained mean thermal expansion coefficients of overheated Ge melt, $\beta_A = 5.94 \times 10^{-5}$ K^{-1} and $\beta_R = 3.10 \times 10^{-5}$ K^{-1} for the range of 1211–1525 K. Similar results were obtained earlier from parabola flight experiments [4, 19].

The change in slope of A/A_0 in the insert of Fig. 18.7d by a factor of two increasing with lower temperatures is very uncommon if compared to a liquid-crystal or liquid-glass transition. Normally, the thermal expansion coefficient decreases at lower temperatures. We also note that we observe this strong increase of the slope from $11.0 \cdot 10^{-5}$ K^{-1} to $21.1 \cdot 10^{-5}$ K^{-1} not in the $Si_{50}Ge_{50}$ alloy (see Fig. 18.7e). A change in the thermal expansion coefficient is most likely coupled to a change in the interatomic potential [21, 22]. This means that the phase transition observed in the liquid could be also reflected in the thermal expansion coefficient here. Further experiments and simulations are necessary to verify this observation.

Nonlinear temperature dependence of the thermal expansion of the melts of Si and Ge was also observed by a thermometric method by Glazov and Shcelikov about 20 years ago [23]. They discussed this behavior in terms of a decrease in the strength of interatomic bonds with increasing temperature. The experimental results are comparable with the behavior of the Ge and SiGe alloy droplets investigated here in the ISS-EML.

In addition, Kulkarni et al. performed ab initio MD simulations of Ge melts [24]. They argue that at lower temperatures, the structure factor shows a pronounced shoulder on the high k-side of the principal peak, which vanishes for high temperatures consistent with experimental scattering data in the literature. The coordination number increases with increasing temperature. This behavior of the structure factor is accompanied by an angle distribution function showing some tetrahedral arrangements at lower temperatures as well [25].

Following Kulkarni et al., our interpretation of the temperature dependence of the volume of the Si-Ge melt states that at very high temperatures, the melt behaves like a simple metallic melt where a linear thermal expansion is expected. With decreasing temperature, covalent, tetrahedral structure elements (small range order) begin to form, and therefore, the specific volume deviates from that of a simple liquid, which is characterized by a simple two-body interatomic potential with linear thermal expansion, leading to the observed nonlinear temperature dependence.

In addition, the solidification of the melt is accompanied by an abrupt increase in A/A_0 and R/R_0 as illustrated in the inset of Fig. 18.4d. The phenomenon can be partly contributed to the volume expansion due to T rise, and partly to the volume anomaly of the substances Si and Ge, whose density in the solid state is lower than that in liquid [4].

9 Electrical Resistivity

The EML levitation facility operating on board the ISS in microgravity (µg) provides a perfect environment for the contactless, inductive measurement of the electrical resistivity of well conducting liquid samples. By application of alternating magnetic fields of high frequency, electromagnetic levitation may stably position and heat conducting samples without external contact by inductive means only. For the handling of the droplets, the EML electromagnetic levitation facility uses a symmetric magnetic quadrupole field produced by two equal, parallel, and coaxial circular RF currents of the same strength but opposite directions to confine the sample against residual disturbances in µg in the center of the coil; see Fig. 18.8.

For an efficient inductive heating and melting of the sample, it applies an additional, widely homogeneous RF magnetic dipole field, generated by two parallel and coaxial circular RF currents of the same strength in the same directions. This "heating field" is simultaneously used as inductive measurement probe.

The almost forceless µg environment provides the advantage that (1) the measurement sample is confined at a fixed place in the coils; (2) the weak applied electromagnetic forces keep the droplet almost spherical and minimize driving turbulent fluid flow in it, which otherwise would result in oscillations of the droplet surface; and (3) the absence of gravity enables a mirror symmetric coil arrangement, which avoids mutual inductive interaction between the electrical heating (measurement) and positioning circuit. The immediate measurement quantity in the present case is the (complex) electrical impedance of the heating circuit $\widetilde{Z}_{tot} = U_0/I_0 e^{i\varphi}$ composed of the amplitude of the RF circuit voltage U_0, the circuit current I_0, and the phase shift φ between both. These three quantities are precisely detected and stored with a data rate of 10 Hz by a dedicated measurement electronics (SCE). After a separate calibration measurement without sample, which yields the impedance of the empty circuit $\widetilde{Z}_{circ}$, the measurement quantity $\widetilde{Z}_{tot}$ enables the determination of
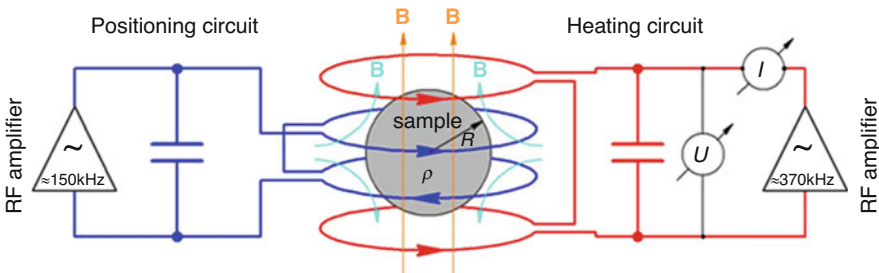

Fig. 18.8 Schematic sketch of the electrical oscillating circuit arrangement of the ISS-EML facility composed of the positioning coil (blue) generating an alternating ($\approx$150 kHz) magnetic quadrupole field (light blue arrows) and the heating coil (red) generating an alternating ($\approx$370 kHz), homogeneous magnetic dipole field (orange arrows). The electrical heating circuit contains an electronic for the precise measurement of the circuit voltage U, current I, and of the phase shift φ between both quantities
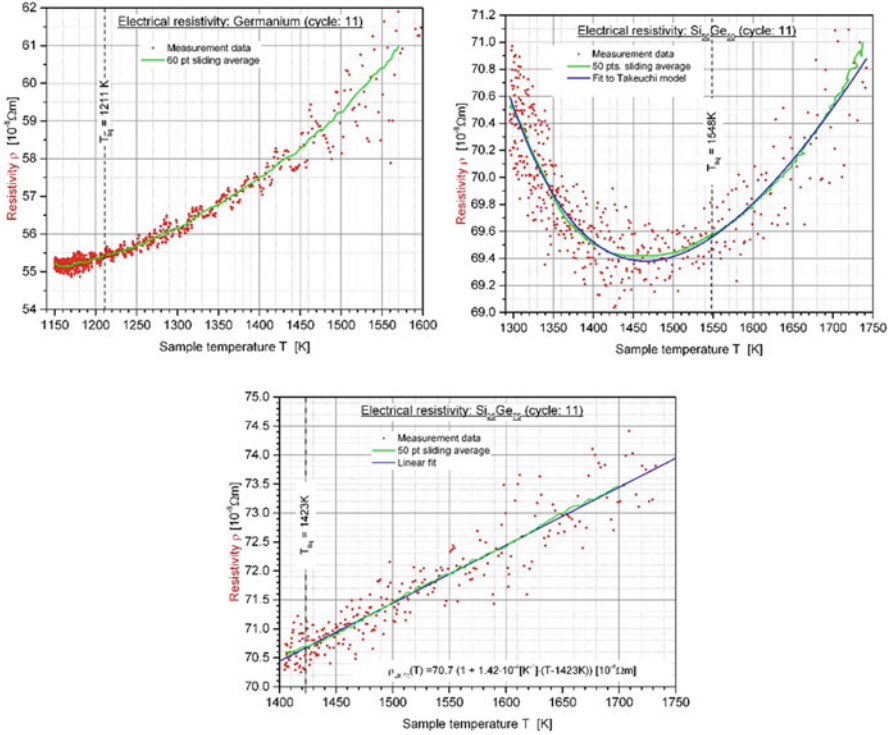
Fig. 18.9 Inductively measured electrical resistivity data (red dots) of liquid germanium, liquid $Si_{50}Ge_{50}$, and liquid $Si_{25}Ge_{75}$ in dependence of the sample temperature above and below the liquidus temperature in the undercooled state. Added are also the sliding averages of the data (green line) and the respective fitted physical models (blue line). (Data for $Si_{50}Ge_{50}$ are taken from Ref. [2])

$\widetilde{Z}_s(R, \rho)$, the contribution to the total impedance from the inductively coupled sample alone. For the simple, clear, and well-defined condition of a spherical sample in a homogeneous magnetic field, provided by the microgravity environment, the physical model derived in [26] allows finally to relate the electrical resistivity $\rho(T)$ and thermal expansion $R(T)$ independently from each other to the real and the imaginary part of $\widetilde{Z}_s(R, \rho)$. A detailed description of the actual levitation and measurement principle is given in Ref. [27].

Within the frame of the "SEMITHERM" project, the temperature-dependent electrical resistivities $\rho(T)$ of liquid germanium and of the two liquid semiconductor alloys $Si_{50}Ge_{50}$ and $Si_{25}Ge_{75}$ have been measured in the EML facility. Levitation and measurement are possible because of the metallic properties of semiconductors in the liquid state. The measurements are performed during the cooling phase of the liquid samples (see Fig. 18.1a) where the magnetic heating field and thus the magnetic forces on the droplets are lowest. The results are collected in Fig. 18.9.

The temperature-dependent electrical resistivity $\rho(T)$ is a sensitive indicator for structural changes in the melt. Generally, the electrical resistivity in liquid metals results from the scattering of the conduction electrons at the disordered metal ions. Accordingly, the decline of the temperature-dependent density fluctuations in the melt with decreasing temperature results in the usually observed linear decrease of ρ [28], a behavior which is shown by the liquid $Si_{25}Ge_{75}$ alloy in the whole measured temperature range; see Fig. 18.9.

In liquid electrically conducting alloys, a formation of compact structures (clusters) with decreasing temperature, due to chemical short-range ordering processes of the components, may result in an increase of the scattering cross section for the electrons and thus of the electrical resistivity [28]. Consequently, an onset of clustering phenomena in a liquid alloy may lead to a deviation of $\rho(T)$ from the typical linear temperature dependence. The lower the temperature of the melt is, the more pronounced this effect should show up. Such a deviation is clearly shown in Fig. 18.9 by both of the other two melts but especially by the present liquid $Si_{50}Ge_{50}$ sample due to its extreme deep undercooling.

Assuming that the $Si_{50}Ge_{50}$ melt can be considered as a regular solution with a positive heat of mixing $W > 0$, meaning that external heat is necessary to keep the liquid alloy components mixed, the unusual temperature behavior of the electrical resistivity can be described by the physical model of Takeuchi and Endo [29]:

$$\rho(x_{Si}, x_{Ge}, T) = \rho_0(x_{Si}, x_{Ge}) + \rho_1(x_{Si}, x_{Ge}) \cdot T + \rho_2(x_{Si}, x_{Ge}) \frac{2x_{Si}x_{Ge}W/RT}{1 - 2x_{Si}x_{Ge}W/RT}$$

where x_{si} and x_{Ge} denote the concentrations of the Si and Ge components (presently $x_{si} = x_{Ge} = 1/2$) and where $\rho_0(x_{si}, x_{Ge})$, $\rho_1(x_{si}, x_{Ge})$, and $\rho_2(x_{si}, x_{Ge})$ are temperature-independent constants. Corresponding to the conventional resistivity model, the above equation contains a constant term and a term which is linearly dependent on the temperature T and dominates for high temperatures. The last term finally considers the increase of the electrical resistivity with decreasing temperature due to the assumed increasing structural evolution of the deeply undercooled $Si_{50}Ge_{50}$ melt by tetrahedral order formation of the Si component. A weighted fit to the measured data points with $\rho_0^{Si,Ge} = 3.5 \times 10^{-5} \Omega$ cm , $\rho_1^{Si,Ge} = 2.2 \times 10^{-8} \Omega$ cm K^{-1}, $\rho_2^{Si,Ge} = 1.6 \times 10^{-5} \Omega$ cm, and $W^{Si, Ge} = 12$ KJ mol^{-1}, which covers the sliding average of the data points fairly well, is shown in Fig. 18.9 in the diagram of $Si_{50}Ge_{50}$. The electrical resistivity data support the interpretation of a structural phase transition in the liquid as discussed in the framework of the thermal expansion measurements.

10   Conclusion

In this work, we report about experiments in the ISS-EML for measurements of the thermophysical properties of highly doped semiconductors Ge, $Si_{25}Ge_{75}$, and $Si_{50}Ge_{50}$. Especially, thermal expansion, surface tension, and damping of the surface oscillations have been investigated.

For the thermal expansion of the melt, we found a nonlinear behavior of the volume as a function of temperature. The findings can be interpreted in terms of a structural change in the melt as a function of temperature. For high temperatures, the melt behaves like a simple metallic fluid with linear thermal expansion. With decreasing temperature, covalent, tetrahedral structure elements (small range order) begin to form, and therefore, the specific volume deviates from that of a simple liquid, which is characterized by a simple two-body interatomic potential with linear thermal expansion, leading to the observed nonlinear temperature dependence.

The surface tension was evaluated using surface oscillations (oscillating drop technique), which were determined with a fast Fourier analysis. The data are in the range of 0.6–0.7 N/m, comparable to previous experiments on parabola flights or in the earth lab and are nearly temperature independent.

The surface oscillations are exponentially damped. For melts showing a laminar flow behavior, the molecular viscosity can be calculated from the damping constant. In our case, however, the flow is turbulent and the damping is related to the flow field of the droplet. The turbulent flow stems from the strong coupling to the positioner field, which is supported by simulations performed in the group of R. Hyers, Univ. of Massachusetts, Amherst. The turbulent behavior could also be observed experimentally by the chaotic movement of small oxide islands on the surface.

The electric resistance of the droplets could be measured inductively by a technique developed by G. Lohöfer, DLR Cologne (sample coupling electronics). For the sample $Si_{50}Ge_{50}$, the resistance as a function of temperature shows a distinct minimum in the undercooled range. For higher temperatures, the resistance increases as expected for simple metallic melts, whereas in the undercooled range, the resistance increases with decreasing temperature. This result supports the interpretation of the thermal expansion data that at lower temperatures, structural changes occur.

In summary, the results of the ISS experiments are very promising, especially the structural changes in the undercooled melt. The data support strongly the idea of a structural phase transition in these melts. Future activities including simulation (R. Maass and P. Derlet) will take a clearer look on the phenomena.

References

1. 25th DLR Parabolic flight campaign, 20th–31st October 2014, Practical and Technical Information, *DI-2014-ed1-en, Novespace, Bordeaux-Mérignac, Mars 2014.* See also: www.novespace.com

2. Y. Luo, B. Damaschke, G. Lohöfer, K. Samwer, Thermophysical properties of a Si50Ge50 melt measured on board the International Space Station. npj Microgravity **6**, 10 (2020) http://creativecommons.org/licenses/by/4.0/

3. N.V. Abrosimov, S.N. Rossolenko, W. Thieme, A. Gerhardt, W. Schröder, Czochralski growth of Si- and Ge-rich SiGe single crystals. J. Cryst. Growth **174**, 182–186 (1997)

4. Y. Luo et al., Contactless processing of SiGe-melts in EML under reduced gravity. npj Microgravity **2**, 1–9 (2016)

5. C.A. Angell, S.S. Borick, Comment on 'Structure of supercooled liquid silicon'. J. Phys. Condens. Matter **11**, 8163–8166 (1999)

6. D. Keren, C. Gotsman, Fitting curves and surfaces with constrained implicit polynomials. IEEE Trans. Pattern Anal. Mach. Intell. **21**(1), 31–41 (1999)

7. W. M. Haynes (ed.), *CRC Handbook of Chemistry and Physics*, 92nd edn. (CRC Press, Boca Raton, 2011) ISBN 1439855110

8. E. Wiberg, N. Wiberg, A.F. Holleman, *Inorganic Chemistry* (Academic/De Gruyter, San Diego/New York/Berlin, 2001) ISBN 0-12-352651-5

9. I. Egry, G. Lohöfer, I. Seyhan, S. Schneider, B. Feuerbacher, Viscosity of eutectic Pd78Cu6Si16 measured by the oscillating drop technique in microgravity. Appl. Phys. Lett. **73**, 462–463 (1998)

10. T. Iwashita, D.M. Nicholson, T. Egami, Elementary excitations and crossover phenomenon in liquids. Phys. Rev. Lett. **110**, 205504 (2013)

11. R.W. Hyers, Fluid flow effects in levitated droplets. Meas. Sci. Technol. **16**, 394–401 (2005)

12. O. Reynolds, An experimental Investigation of the circumstances, which determine whether the motion of water shall be direct or sinuous, and of the law of resistance in parallel channels. Philos. Trans. R. Soc. Lond. **174**, 935–982 (1883)

13. Z. Zhou, S. Mukherjee, W.K. Rhim, Measurement of thermophysical properties of molten silicon using an upgraded electrostatic levitator. J. Cryst. Growth **257**, 350–358 (2003)

14. J.J.Z. Li, W.K. Rhim, C.P. Kim, K. Samwer, W.L. Johnson, Evidence for a liquid–liquid phase transition in metallic fluids observed by electrostatic levitation. Acta Mater. **59**, 2166–2171 (2011)

15. G. Bracker et al., *Reported on the 12th International Workshop on Subsecond Thermophysics* (IWSSTP 2019), hold June 3–6, 2019, Cologne, Germany

16. I. Egry, On the relation between surface tension and viscosity for liquid metals. Scripta Met. Mat. **26**, 1349 (1992)

17. J. Brillo, *Thermophysical Properties of Multicomponent Liquid Alloys, De Gruyter Oldenbourg* (Walter de Gruyter GmbH, Berlin/Boston, 2016)

18. X. Xiao, R.W. Hyers, R.K. Wunderlich, H.J. Fecht, D.M. Matson, Deformation induced frequency shifts of oscillating droplets during molten metal surface tension measurement. Appl. Phys. Lett. **113**, 011903 (2018)

19. S.M. Chathoth, B. Damaschke, K. Samwer, S. Schneider, Thermophysical properties of Si, Ge, and Si–Ge alloy melts measured under microgravity. Appl. Phys. Lett. **93**(1–3), 071902 (2008)

20. E. Ricci et al., Surface tension and density of Si-Ge melts. J. Chem. Phys. **140**, 214704 (2014)

21. D.S. Sanditor, A criterion for the glass-liquid transition. J. Non-Cryst. Solids **385**(148) (2014)

22. V.A. Drebushchak, A.I. Turkin, Relationship between heat capacity and thermal expansion derived from the Lennard–Jones potential. J. Therm. Anal. Calorim. **65**, 745–753 (2001)
23. O.V. Glazov, M.D. Shchelikov, Volume changes during melting and heating of silicon and germanium melts. High Temp. **38**, 405–412 (2000)
24. R.V. Kulkarni, W.G. Aulbur, D. Stroud, Ab initio molecular-dynamics study of the structural and transport properties of liquid germanium. Phys. Rev. B **55**, 6896 (1997)
25. S.M. Chathoth, B. Damaschke, T. Unruh, K. Samwer, Influence of structural changes on diffusion in liquid germanium. Appl. Phys. Lett. **94**, 221906 (2009)
26. G. Lohöfer, Magnetization and impedance of an inductively coupled metal sphere. Int. J. Eng. Sci. **32**, 107–117 (1994)
27. G. Lohöfer, High-resolution inductive measurement of electrical resistivity and density of electromagnetically levitated liquid metal droplets. Rev. Sci. Instrum. **89**, 124709 (2018)
28. S. Takeuchi, H. Endo, The electrical resistivity of the metals in the molten state. Trans. JIM **3**, 30–35 (1962)
29. S. Takeuchi, H. Endo, Theoretical and experimental studies on the resistivity of molten alloys. Trans. JIM **3**, 35–41 (1962)